



HAL
open science

Using a bio-inspired copper complex to investigate reactive mass transfer around an oxygen bubble rising freely in a thin-gap cell

Francisco Felis, Florian Strassl, Larissa Laurini, Nicolas Dietrich, Anne-Marie Billet, Véronique Roig, Sonja Herres-Pawlis, Karine Loubiere

► To cite this version:

Francisco Felis, Florian Strassl, Larissa Laurini, Nicolas Dietrich, Anne-Marie Billet, et al.. Using a bio-inspired copper complex to investigate reactive mass transfer around an oxygen bubble rising freely in a thin-gap cell. *Chemical Engineering Science*, 2019, 207, pp.1256-1269. 10.1016/j.ces.2019.07.045 . hal-02272722

HAL Id: hal-02272722

<https://hal.science/hal-02272722>

Submitted on 28 Aug 2019

HAL is a multi-disciplinary open access archive for the deposit and dissemination of scientific research documents, whether they are published or not. The documents may come from teaching and research institutions in France or abroad, or from public or private research centers.

L'archive ouverte pluridisciplinaire **HAL**, est destinée au dépôt et à la diffusion de documents scientifiques de niveau recherche, publiés ou non, émanant des établissements d'enseignement et de recherche français ou étrangers, des laboratoires publics ou privés.







Open Archive Toulouse Archive Ouverte

OATAO is an open access repository that collects the work of Toulouse researchers and makes it freely available over the web where possible

This is an author's version published in: <http://oatao.univ-toulouse.fr/24196>

Official URL: <https://doi.org/10.1016/j.ces.2019.07.045>

To cite this version:

Felis, Francisco  and Strassl, Florian and Laurini, Larissa and Dietrich, Nicolas and Billet, Anne-Marie  and Roig, Véronique  and Herres-Pawlis, Sonja and Loubière, Karine  *Using a bio-inspired copper complex to investigate reactive mass transfer around an oxygen bubble rising freely in a thin-gap cell.* (2019) *Chemical Engineering Science*, 207. 1256-1269. ISSN 0009-2509

Any correspondence concerning this service should be sent to the repository administrator: tech-oatao@listes-diff.inp-toulouse.fr

Using a bio-inspired copper complex to investigate reactive mass transfer around an oxygen bubble rising freely in a thin-gap cell

Francisco Felis^{a,e}, Florian Strassl^d, Larissa Laurini^d, Nicolas Dietrich^b, Anne-Marie Billet^a, Véronique Roig^c,
Sonja Herres-Pawlis^d, Karine Loubière^{a,*}

^aLaboratoire de Génie Chimique, Université de Toulouse, CNRS, INPT, UPS, Toulouse, France

^bToulouse Biotechnology Institute Bio & Chemical Engineering (TBI), Université de Toulouse, INRA, INSA, Toulouse, France

^cInstitut de Mécanique des Fluides de Toulouse (IMFT), Université de Toulouse, CNRS, INPT, UPS, Toulouse, France

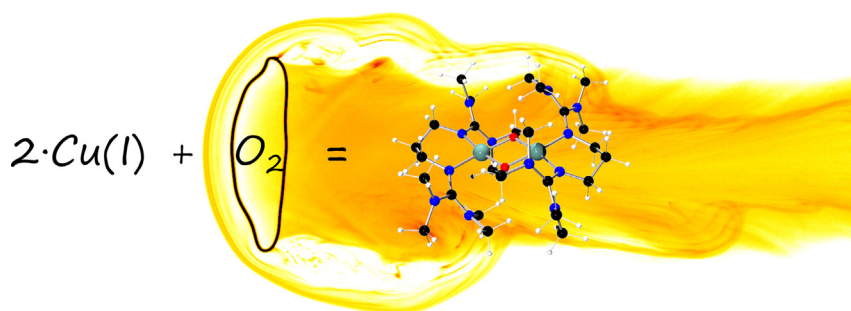
^dRWTH Aachen University, Institut für Anorganische Chemie, 52074 Aachen, Germany

^eFédération de Recherche FERMAT, CNRS, Toulouse, France

HIGHLIGHTS

- Bio-inspired copper complexes are tailored to explore reactive gas-liquid mass transfer.
- Single pure oxygen bubbles are generated in a thin-gap cell which gap is 1 mm.
- Gap- and time-averaged oxygen concentration fields are measured in the far-field wake.
- A representation Sherwood-Peclet enables to gather the results.
- Intrinsic Sherwood numbers can be determined from the calculated enhancement factor.

GRAPHICAL ABSTRACT



ABSTRACT

The present study describes an original colorimetric method to visualize and quantify the local oxygen mass transfer around a rising bubble in reactive media. This method is based on the use of a colorless bio-inspired copper complex, $\text{Cu}(\text{btmgp})\text{I}$, specially tailored for the study, which, dissolved in acetonitrile, oxidizes into an orange copper-complex $[\text{Cu}_2\text{O}_2(\text{btmgp})_2]_2$. The latter complex, unstable at ambient temperature, decays quite fast into two $\text{Cu}(\text{II})$ complexes, leaving a permanent pale-green color as final products. The flow investigated consists in a pure oxygen single bubble rising freely in a confined thin-gap cell ($400 \times 200 \times 1$ mm). A wide range of motion regimes for the bubbles are observed as the Archimedes number ranges from $860 < Ar < 18,800$ and the Reynolds number from $580 < Re < 8200$. A high-resolution 16-bit sCMOS camera, combined with specific filters, is used to capture images from a region-of-interest of the cell, illuminated by a white LED backlight panel. An ad hoc calibration protocol is developed to correlate the grey-levels from the colored signal to the equivalent oxygen concentrations. This procedure then allows to measure indirectly the amount of oxygen transferred to the liquid phase. The series of images are also treated to identify the bubble motion and properties. Thanks to this method, equivalent oxygen concentration fields, gap-averaged and time-averaged, can be reached with high precision in the far-field wake of the bubbles, enabling thus to deeply characterize the mass transfer mechanisms under reactive conditions in such confined configuration, and to establish a dimensionless representation in terms of Sherwood number versus Peclet number. At last, thanks to the knowledge

Keywords:

Reactive bubbly flows
Mass transfer
Bioinspired copper complex
Thin-gap cell
Experimental imaging

* Corresponding author.

E-mail address: karine.loubiere@ensiacet.fr (K. Loubière).

Nomenclature

A	absorbance signal, dimensionless	<i>Greek letters</i>	
$[C]$	initial concentration of Cu(I)-complex, kg m^{-3}	μ_L	liquid dynamic viscosity, Pa s
$C_{O_2}^*$	concentration of dissolved oxygen at saturation, kg m^{-3}	φ	mass flux of oxygen transferred, kg s^{-1}
C_{O_2}	equivalent oxygen concentration in the liquid phase, kg m^{-3}	ϕ	mass flux density of oxygen transferred, $\text{kg m}^{-2} \text{s}^{-1}$
C_{Cu}	initial concentration in Cu complex in the liquid phase, kg m^{-3}	ρ_L	liquid density, kg m^{-3}
d	bubble diameter defined in Eq. (1), m	σ	surface tension, N m^{-1}
\mathcal{D}	diffusion coefficient, $\text{m}^2 \text{s}^{-1}$	<i>Dimensionless numbers</i>	
g	gravity constant, m s^{-2}	Ar	Archimedes number (Eq. (7))
I	is the 16-bit pixel-by-pixel intensity, dimensionless	Bo	Bond number (Eq. (7))
m	mass of oxygen deposited, kg	Pe	Peclet number (Eq. (15))
M	molar mass, g mol^{-1}	Re	Reynolds number (Eq. (8))
S	bubble plane projected area, m^2	Sh	Sherwood number (Eq. (14))
S_T	total area of the bubble gas-liquid interface defined as $S_T = S_p + S_f$, m^2	We	Weber number (Eq. (8))
S_p	area of the peripheral interface in contact with the in-plane flow (Eq. (3), Fig. 2b), m^2	χ	bubble aspect ratio
S_f	areas of the liquid film (Eq. (3), Fig. 2b), m^2	<i>Subscript</i>	
T	transmittance signal, dimensionless	b	bubble
V_b	mean bubble velocity defined in Eq. (2), m s^{-1}	Cu	Cu(I)-complex
		O_2	oxygen
		x	x-axis
		w	water

of the kinetic rate of the reaction and of the diffusion coefficients, the Hatta number and the enhancement factor are estimated, and thus the intrinsic Sherwood numbers; these results demonstrate that the enhancement of the mass transfer by the reactions involved with the copper-complexes is not negligible (almost 12–15%).

1. Introduction

Reactive bubbly flows are involved in a broad portfolio of industrial processes such as petrochemical, cosmetics, mineral processing, wastewater treatment, and many chemical and biochemical processes. Consequently, the analysis of transport phenomena between the participating phases is a crucial task of recent and prospective research. Particularly, the understanding of mass transfer mechanisms across gas-liquid interfaces is of high importance to optimize production processes, but also to find new ways to increase their performances. During the last decades, cutting-edge production technologies for process intensification, such as heat-exchanger-reactor, monolith reactor, flat photo-(bio-) reactor, have emerged as alternatives to conventional equipment (such as bubble column). They are particularly interesting for carrying out gas-liquid reactions as they involve confined configurations, thus offering enhanced heat and mass transfer, efficient mixing, and high interfacial area (Anxionnaz et al., 2008; Martinez et al., 2016; Pruvost et al., 2017).

In this study, special attention is paid to an in-plane confined bubbly flow which covers an intermediate configuration between large bubble column and Taylor flow. Here, bubbles are injected in a vertical planar thin-gap cell filled with liquid at rest which gap size is smaller than bubble diameters. The bubbles rise at high Reynolds number and they are surrounded by thin lubrication films between their interface and the walls of the cell. This particular confinement in a plane enables to enhance mass transfer as compared to 3D bubble columns (Roudet et al., 2017) and also enhances mixing as compared to Taylor flows. At high Schmidt number, mixing in the liquid phase is favored by possible transport

of dissolved concentration by the in-plane bubble-induced agitation. This specific agitation and the associated mixing mechanisms have been described in a homogeneous bubbly flow by Bouche et al. (2012, 2014) and Almeras et al. (2016, 2018). An additional advantage of this confined configuration is to offer the possibility to cover a wide range of motion regimes for the bubbles and of subsequent mass transfer regimes. Such confined bubble reactors also find promising applications, in particular towards light-activated reactions, such as the synthesis of added-value molecules by photochemical pathways (Oelgemöller, 2016), the cultivation of microalgae (Pruvost et al., 2017; Thobie et al., 2017) or the methane formation from carbon dioxide (Rao et al., 2017). Due to the light attenuation and to the absorbing nature of the medium, the latter applications need photoreactors with narrow geometry to be designed, while offering efficient mixing and mass transfer.

Experimental investigation of interfacial mass transfer at the local scale (around a bubble) is nowadays possible for pure (non-reactive) mass transfer, and even in the presence of a chemical reaction. However, the related works are still rare, mainly due to technical difficulties.

Among the different techniques, the Planar Laser-Induced Fluorescence with Inhibition (PLIFI) technique stands out as an efficient method to access oxygen concentration fields and thus to quantify mass transfer in bubbly flows. As its principle does not involve a chemical reaction (but a photophysical process), PLIFI technique can be used to characterize non-reactive mass transfer. This has been done by Rüttinger et al. (2018), by Butler et al. (2016, 2018) in Taylor flows and by Jimenez et al. (2013) in the wake of non-spherical air bubbles. Roudet et al. (2017) have also used PLIFI to study the influence of confinement on the mass transfer of freely

rising oxygen bubbles confined in a vertical thin-gap cell. Even if a convincing scaling law relating the mass transfer rate to the hydrodynamics, $Sh Pe^{0.5}$, was provided (where Sh is the Sherwood number and Pe the Peclet number), this investigation has to be continued. Indeed, it gave access to time-averaged fluorescence fields in the liquid phase far from the bubble that are not easy to correlate to the oxygen concentration distribution without strong assumptions. In addition, interfacial mass transfer under reactive conditions is important to explore towards industrial applications.

To provide an alternative to the PLIFI, colorimetric techniques are available to investigate primarily the reactive mass transfer but also to evaluate the non-reactive one. They involve at least one given chemical reaction between the molecule transferring at the gas-liquid interface and another molecule present in the liquid phase (often a dye), which leads to the formation of a colored product. Measurements are based on the establishment of a calibration curve relating the color level to the concentration of the product, and then, using the reaction stoichiometry, to the “equivalent” concentration of the molecule of interest that has been transferred to the liquid phase. Some caution should be taken when using this technique. For instance, one has to ensure, by a proper choice of operating conditions, that all the molecules of interest (i.e. the transferred molecules) are consumed by the reaction in the liquid phase so as to guarantee that the method provides a correct evaluation of mass transfer. The initial concentration of the dye has thus to be large enough.

As these colorimetric methods involve chemical reactions, they give access to the reactive mass transfer related to a bubble flow and to a liquid phase (reactional mixture) of given physico-chemical properties. Experimentally, it is not thus possible to perform a direct measurement of pure physical mass transfer - that is without reaction - for this bubbly flow. However, for industrial applications, one has to quantify the impact of the chemical reaction on mass transfer as compared to pure physical absorption configuration. For this purpose, the concept of enhancement factor E has been introduced to estimate the mass transfer in the presence of any reaction. This factor E is defined as the ratio between the interfacial mass transfer rate and the one existing in the absence of chemical reaction (Roizard et al., 1997; Levenspiel, 1999). It is calculated by solving a set of equations (established from several assumptions), involving various dimensionless numbers - depending on the chemical regime -, including the Hatta number. Such accurate local experimental investigations of reactive mass transfer are also necessary to go along with promising numerical simulations that aim at tackling with complex coupling (see among other researches for example: Khinast, 2001; Radl et al., 2008; Falcone et al., 2018).

The first colorimetric technique used in our team was developed by Dietrich et al. (2013) to study the mass transfer around Taylor bubbles flowing in a square millimetric channel. The technique is based on the use of a reversible oxido-reduction reaction: a dye called resazurin, which is colorless in an oxygen-free medium, consumes, in presence of glucose and sodium hydroxide, the species of interest (i.e. oxygen), revealing a colored (pink) product in the visible spectrum. The measurement is then performed by tracking the reaction product (named resorufin) using a high-speed camera set-up and a visible-light source (no laser is required when compared to PLIFI). Moreover, Yang et al. (2017) determined the associated kinetic constant and diffusion coefficients, making possible the calculation of the enhancement factor (E) in this bubbly flow; for their specific conditions, they showed that $E \approx 1$, meaning thus that this chemical reaction used for the colorimetric measurements does not enhance the mass transfer rate of oxygen at the interface (note that when $E \neq 1$, one should correct the

measured mass transfer rate by the factor of E). This technique was later used by other authors, such as Kováts et al. (2018) in a helically coiled pipe.

Recently, other colorimetric methods appeared. Paul et al. (2018) summarized that coordination chemistry had given new impulses to study the mass transfer in reactive bubbly flows, in particular due to the possibility to synthesize tailored complex systems for the detection of O_2 and NO with various time- and space-resolved techniques. Especially the ligands were highlighted for their ability to fine-tune the reactions and their kinetics. Many of these systems are bioinspired since nature has evolved methods over a long period of time to come along with difficult gases such as O_2 and NO (Kroneck and Sosa Torres, 2015): Copper metalloproteins activate dioxygen for oxygen transport (as found in hemocyanin in arthropods and molluscs) and transfer to organic substrates (as found in tyrosinase, used for browning processes in fruits, hair and feathers) (Solomon et al., 2014). In the last decades, a plethora of synthetic model complexes for tyrosinase have been reported which transfer the biological activity into a non-protein context (Citek et al., 2015; Hamann et al., 2017; Liebhäuser et al., 2016). In few cases, the hydroxylation activity is enhanced compared to the biological system (Hoffmann et al., 2013; Wilfer et al., 2015; Liebhäuser et al., 2017). In particular, Kastens et al. (2017) investigated gas-liquid reactive mass transfer around Taylor bubbles. Experiments were carried out using simple $Cu(I)$ ammonia complexes that reacted with oxygen and turned from colorless to deep blue. Different wake structures behind the bubbles were observed by PIV, and depending on them, various colored concentration fields were obtained. The authors showed how the wake structure could affect the yield and the selectivity of chemical reactions. Nevertheless, these colored concentration fields were not quantitatively correlated to the transferred oxygen concentration, and therefore the calculation of Sherwood numbers was not possible.

In keeping with this context, the present study aims to locally visualize and quantify the oxygen mass transfer around a single pure oxygen bubble freely rising at large Reynolds number in a vertical thin-gap cell where the liquid phase is at rest, and under reactive conditions. For this purpose, a colorimetric method is implemented, based on the use of a colorless bio-inspired copper complex, $Cu(btmgp)l$, specially-tailored for the study, which is dissolved in acetonitrile and produces an orange $Cu(III)$ complex when in contact with oxygen; the latter is then transformed into a mixture of two $Cu(II)$ complexes. The present investigation is complementary with the work of Roudet et al. (2017) as the physico-chemical properties of the liquid mixture are different in both studies, thus changing bubble shapes and motion for a given gas volume. Moreover, an original chemical reaction with known kinetics is used for the first time for studying reactive mass transfer in this particular confined thin-gap bubbly configuration. Then, the objectives of this work are both to present an original method for quantitative analysis of reactive mass transfer and to show the relationship between reactive and non-reactive gas-liquid mass transfer that this method makes possible to establish.

Section 2 will describe the materials and methods, in particular the chemical system involved, the experimental set-up and the image acquisition system. In Section 3, the implementation of the colorimetric technique will be presented in detail: based on the development of a custom image processing to be applied to the raw images along with an ad-hoc calibration procedure, it will allow to track the bubbles and their motion, as well as to match the grey-levels of the acquired images with the equivalent oxygen concentration. Section 4 will be devoted to the results and discussion: the dynamics of the bubbles generated will be first analyzed, the equivalent oxygen concentration fields determined

will be discussed under the light of bubble dynamics. At last, all the results will be gathered on a representation plotting the Sherwood number as a function of the Peclet number, and the enhancement factor will be estimated so as to evaluate the non-reactive mass transfer.

2. Materials and methods

2.1. Chemical system

The chemical system used herein involves the Cu(btmgp)I complex from the original work of Herres-Pawlis et al. (2005a). It is initially dissolved in oxygen-free pure acetonitrile (Chromasolv™ Gradient Grade, CAS 75-05-8, purity $\geq 99.9\%$) and is colorless. When reacting with oxygen, the Cu(I) complex oxidizes into a Cu(III) complex of orange color. However, the latter complex is not stable at ambient temperature (Herres-Pawlis et al., 2005b) and decays quite fast (in almost few seconds at ambient temperature, as shown later in Fig. 5) into two Cu(II) complexes, leaving a permanent pale-green color as final products. The reaction is not reversible, making the post-processing of the experiments more challenging. This consecutive reaction scheme is described in Fig. 1.

The Cu(I) complex is synthesized according to the reported procedure (Herres-Pawlis et al., 2005b).

The physical properties of this reaction medium are assumed identical to the ones of the solvent (pure acetonitrile). At 20 °C, the liquid density is thus taken equal to $\rho_L = 779.3 \text{ kg m}^{-3}$, the liquid dynamic viscosity to $\mu_L = 0.37 \text{ mPa s}$, and the surface tension to $\sigma_L = 28.6 \text{ mN m}^{-1}$. The diffusion coefficient and solubility of pure oxygen in acetonitrile are $\mathfrak{D}_{O_2} = 9.2 \times 10^{-9} \text{ m}^2 \text{ s}^{-1}$ and $C_{O_2}^* = 259 \text{ mg L}^{-1}$ (Achord and Hussey, 1980; Li et al., 2013).

2.2. Experimental set-up

A specific set-up has been built to experimentally investigate the interfacial mass transfer of oxygen around a single bubble of pure oxygen, freely rising at high Reynolds number in a planar vertical thin-gap cell, which is previously filled with an oxygen-free reactive liquid solution.

Schematic representations and pictures of the experimental set-up are shown in Figs. 2 and 3a. The thin-gap cell is made of two optical-grade glass plates having a height and width, H and W , equal to 400 and 200 mm respectively, and separated by a nominal thin gap of width h equal to 1 mm. The latter was accurately assessed using a Confocal Laser Scanning Microscope (CLSM) and found equal to $h = 1.062 \pm 0.005 \text{ mm}$. The glass plates are mounted on a stainless-steel structure in order to be compatible with the reaction medium, the sealing of the whole system being guaranteed by custom made gaskets.

When the liquid phase is at rest, a single pure oxygen bubble is released by means of a burst valve opening (manual operation) from a small silica capillary tube (0.5 mm in diameter 20 mm in length) centered at the bottom of the planar vertical thin-gap cell as Fig. 2 shows. The bubble size cannot be controlled (it depends on how the valve is manually opened), thus making necessary to determine it *a posteriori* by means of image processing.

Various sets of stainless-steel tubes, valves, flowmeters and pressure sensors, combined with two gastight vessels (also made of stainless steel, see Fig. 3a), are placed upstream the cell and enable to:

- inject either pure oxygen or nitrogen (the latter being used to initially mix the solution in the cell);

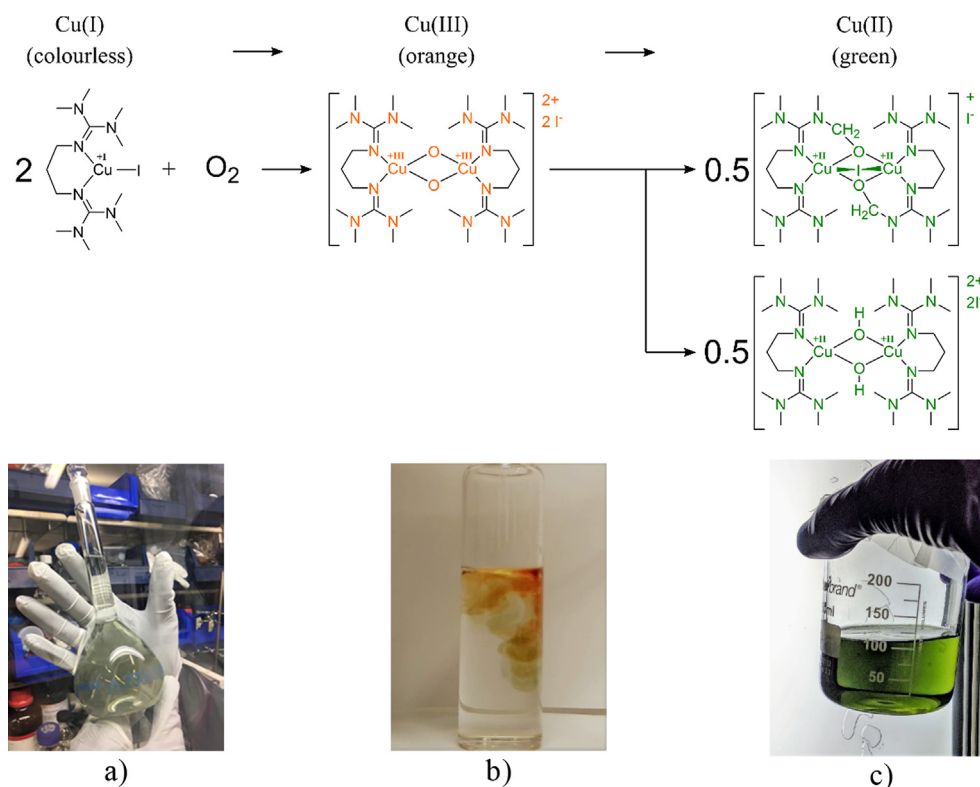


Fig. 1. Chemical system involving the Cu(btmgp)I copper-complex. (a) Colorless Cu(I) prepared in an oxygen-free argon glove-box. (b) Open bottle visualization of the orange Cu(III) reaction with air. (c) Final product of the reaction, green Cu(II). (For interpretation of the references to color in this figure legend, the reader is referred to the web version of this article.)

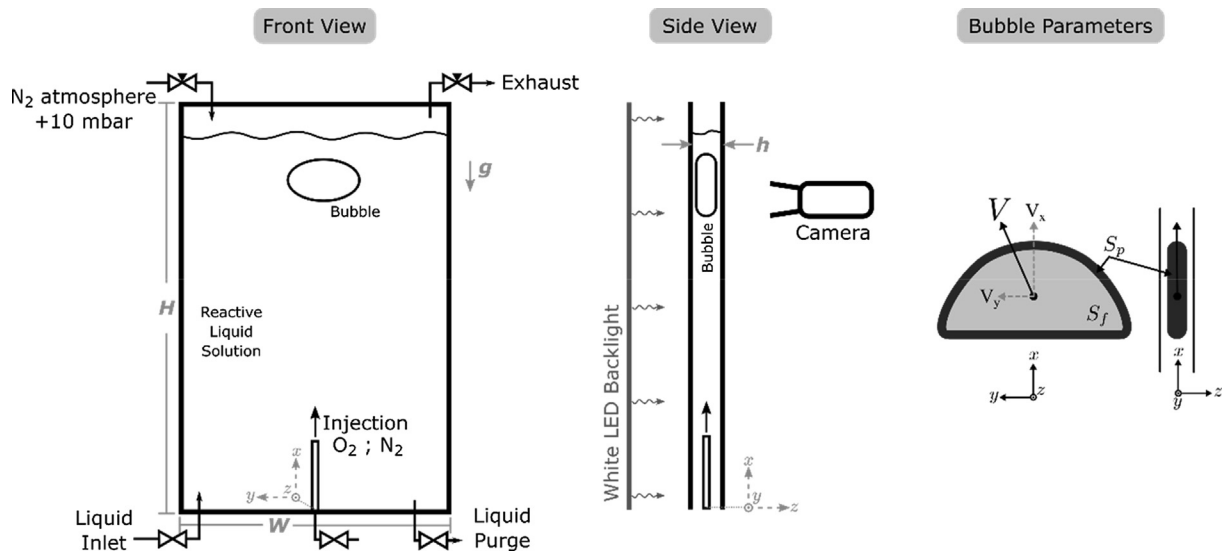


Fig. 2. Schematic representations (not-to-scale) of the experimental set-up. Main fluid circuits and geometrical parameters of the Hele-Shaw cell and the measured bubbles are shown.



Fig. 3. Pictures of the experimental set-up: (a) Panoramic view. (b) Gastight vessels made of stainless steel (one containing the cleaning solution and the other the initial Cu(I)-complex solution).

- fill the cell with the oxygen-free reaction medium (namely acetonitrile with a given concentration of Cu(I) complex);
- clean the cell with pure solvent. Note that this operation should be done after each time that an oxygen bubble is injected and transferred oxygen into the liquid phase, as the reaction with the copper complexes is not reversible.

The solution containing Cu(I) complex in acetonitrile is prepared under argon atmosphere in a glovebox and transferred into the gastight vessel. This vessel can then be connected to the set-up without any contact with oxygen thanks to the nitrogen purge circuit (Fig. 3b).

2.3. Image acquisition system

The motion of the bubble, its shape oscillations and the oxygen concentration are measured using an imaging system. The latter consists of a collimated white LED backlight panel (PHLOX, $400 \times 200 \text{ mm}^2$) that illuminates the cell from behind. A 16-bit

sCMOS PCO Edge $2560 \times 2160 \text{ px}$ camera equipped with a 50 mm 1:12 Nikkor lens is placed in front of the cell. Time-series of grey-level images at 100 Hz (exposure time 0.8–1 ms) are captured (almost 580–680 images), the scale ratio being of 14.627 px/mm. These acquisition parameters are set to generate images with both wide response range in the 16-bit grey-levels and sharp enough contours to accurately detect the bubbles borders and concentration field around and in the wake of the bubble.

The first implemented method provides a qualitative analysis on the formation of the orange Cu(III) complex, right next to the oxygen bubble interface and in the near-field wake. Using an analogy from transmissive media, to increase the contrast ratio of the grey-levels seen by the camera when an orange signal is present, a narrow blue band-pass filter is added (TECHSPEC[®] by Edmund Optics, CWL 470 nm, OD ≥ 3.0 @ 200–400 nm, OD ≥ 4.0 @ 550–1200 nm) as this color is complementary to the orange signal present in the experiments. The second implemented method is devoted on the contrary to quantify the actual amount of final green reactive Cu(II) complexes in the far-field wake: a red band-pass filter is then used

(TECHSPEC[®] by Edmund Optics, CWL 660 nm, OD \geq 3.0 @ 200–550 nm, OD \geq 4.0 @ 720–1120 nm). This last filter allows making the green reactive Cu(II) complexes transported in the wake visible even several seconds after its apparition.

A unique region-of-interest (ROI) window is used for all the bubbles. The ROI's dimensions are 175.02×61.53 mm (2560×900 px) in x and y vertical and horizontal directions. It is horizontally centered in the cell and located at 700 mm from the top, enabling to follow the bubbles after reaching a stationary motion, far from the transient effects due to bubble formation, and also before getting disturbed by the vicinity of the free-surface at the top.

3. Implementation of the colorimetric technique

A custom image processing on the raw images and an ad-hoc calibration procedure have been developed. They allow to track the bubbles and their motion, and to interpret the grey-levels observed on the acquired images as equivalent oxygen concentration C_{O_2} .

3.1. Image processing

The algorithm is built using MATLAB[®] along with the *Image Processing Toolbox* package. An edge detection filter based on the Otsu's method (Otsu, 1979) and temporal tracking allow to obtain several bubble properties: the in-plane projected area S , the perimeter of this projected surface, P , the velocity, V_b , and the associated x - and y -components, V_x and V_y , and the aspect ratio, χ (see Fig. 2). The bubble size is characterized by the in-plane equivalent diameter, d , defined as:

$$d = \sqrt{\frac{4S}{\pi}} \quad (1)$$

The aspect ratio of the bubble χ , is calculated as the ratio of the major and minor axis of the ellipse of identical moments of inertia as the projected 2D bubble.

The mean bubble velocity V_b , is defined by averaging over time the vertical velocity of the bubble (for a whole number of periods when the motion is periodic). Denoting $\langle \cdot \rangle$ the averaging operator we write:

$$V_b = \langle V_x \rangle \quad (2)$$

Mass transfer happens in regions of contrasted hydrodynamics: in the liquid films in between the bubble and the walls which area for one film is denoted S_f , and at the peripheral interface in contact with the in-plane flow, of area S_p (see Fig. 2). Both areas have to be evaluated, as the bubble does not touch the glass surface and is completely surrounded by the reactive liquid media. Considering lubrication films, their thickness h_f is negligible as compared to h (their ratio is around 1% as estimated from Bretherton's theory (Aussillous and Quéré, 2000)), therefore the measurements of the in-plane projected area S and of the perimeter of this projected surface P , provide the estimation of S_f and S_p :

$$S_f = 2S \text{ and } S_p = hP \quad (3)$$

In addition to the calculation of bubble characteristics, the algorithm can detect the field of grey-levels observed on the images, in the vicinity and in the wake of the bubble, which is related to the equivalent concentration of oxygen transferred from the bubble to the liquid phase, C_{O_2} . Fig. 4 shows a series of raw images captured in the region-of-interest (see videos on supporting information). Without any further analysis, one can visualize the type of wake

left by the reactive mass transfer behind the rising bubble, the shape of the gas-liquid interface and from temporal records the bubble motion for bubbles of various volumes.

From a qualitative point-of-view, to clearly visualize the reaction from the orange Cu(III) to the green Cu(II), the actual temporal and spatial evolutions of grey-levels (GV) are extracted along line A (transversal) and line B (axial) in the wake of a bubble (see Fig. 4d). The resulting transversal and axial GV profiles are plotted in Fig. 5. Note that, using the blue-filter, the contrast ratio on Cu(III) concentration is enhanced, so GV are here mainly related to the presence of the Cu(III) species, and the Cu(II) is barely visible after the reaction is complete. Fig. 5a shows transversal profiles in the laboratory frame (along line A), corresponding to various time instants. Such characteristic bimodal shape was already observed by Roudet et al. (2017) on time-averaged PLIF signals and in the absence of any chemical reaction. However, their temporal evolution can be observed here, while the reaction is occurring, from the bubble crossing instant, up to several seconds after. The profiles evolve during time due to either the motions in the liquid or the chemical reaction (this is illustrated by the movies provided as supporting information). The motions in the liquid are damped due to the shear stress at the walls in a viscous characteristic time scale $\tau_v = h^2/4\nu_l$ of about 0.6 s (where ν_l is the kinematic viscosity) (Roig et al. 2012). The decrease of the GV is then strongly linked to consumption of the orange Cu(III) complex. Once the latter is totally transformed into Cu(II) complexes, the profiles in Fig. 5a stabilize. The convergence of this temporal evolution is then emphasized in Fig. 5b where GV data are extracted at the intersection of lines A and B ($y = 250$ px), showing their evolution along time in the laboratory frame (i.e. along the bubble wake). On the basis of the calculated exponential decay rate of 2.5 s^{-1} (i.e. the parameter β of the equation related to the identified curve fitting, see Fig. 5b), a vanishing time of ~ 2.5 s can be deduced, corresponding to the moment where 99% of the asymptote value is reached. This last piece of information assesses the later calibration procedure, as it proves that, after ~ 2.5 s, no Cu(III) complex is present, and everything has been converted into the stable state Cu(II). This characteristic time can be adopted for all experiments, as it was processed in a case of elevated mass-transfer flux (bubble "d" shown in Fig. 4). One should note that it is in agreement with the characteristic times obtained by Schurr et al. (2016).

Also linked to the raw images, Fig. 5c shows the instantaneous grey-level profile along line B from Fig. 4d after the background image is removed. Three zones can be identified:

- first, the halo at the front of the bubble (blue curve) already observed during non-reactive transfer (Roudet et al., 2017),
- then the mass transfer inside the liquid films that explains the increase of GV observed through the bubble (orange curve),
- and finally, the wake behind the bubble (grey curve), which presents first an increase of GV due to collection of the Cu(III) complex by the flow near the bubble and then a decrease due to the conversion from Cu(III) into Cu(II) complexes along time.

Note that the two undefined sections between these zones correspond to the area of the bubbles interface.

3.2. Calibration curve for oxygen measurements

As in the method proposed by Dietrich et al. (2013) with resazurin dye, an indirect calibration is performed, where each grey-level pixel is associated with a gap-averaged equivalent oxygen concentration C_{O_2} via an empirical relationship, named calibration curve. It is important to keep in mind that the term "gap-averaged" means that the concentration is averaged along the z -direction

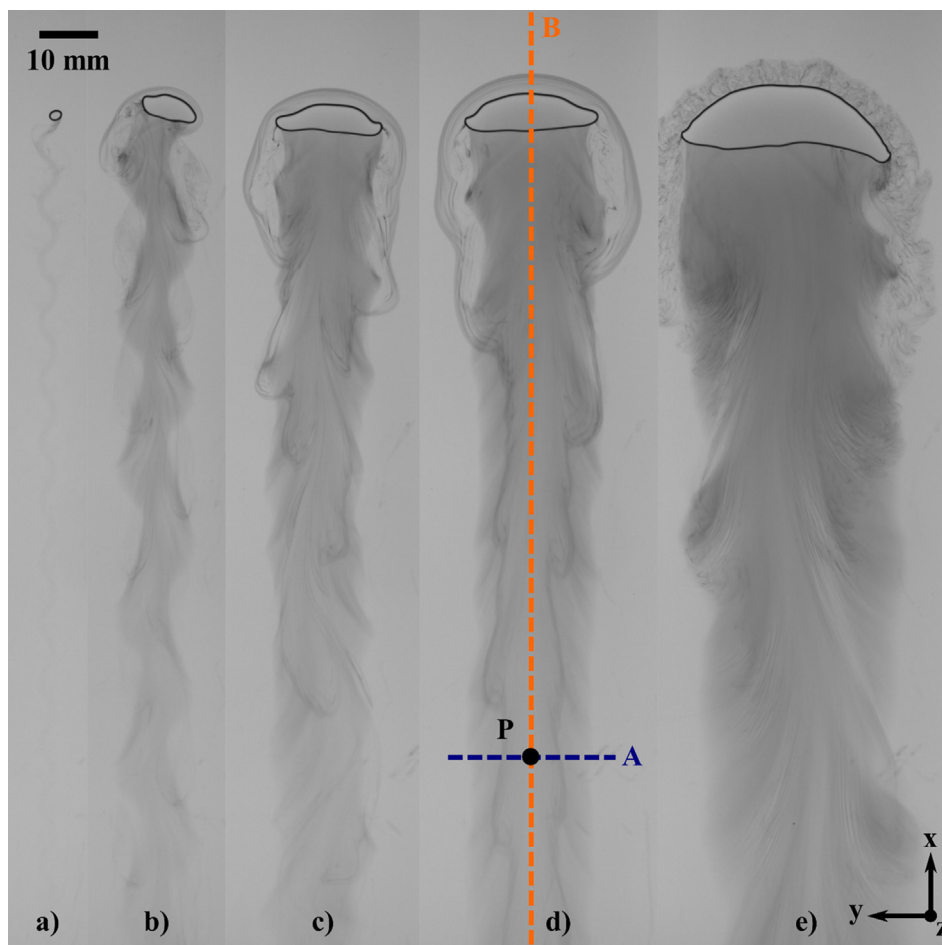


Fig. 4. Raw images of the reactive visible color signal in the wake of bubbles of different sizes. A blue band-pass filter was used to increase the signal issued from the orange Cu(III)-complex near the bubbles. (For interpretation of the references to color in this figure legend, the reader is referred to the web version of this article.)

(that is to say along the gap thickness, h), and that the calibration is valid only for a given geometry, imaging and lighting conditions.

The calibration procedure consists in completely saturating the copper complex solution inside the cell by flushing it with pure oxygen for a certain time, until all the copper complex has reacted. This procedure is carried out at several initial concentrations of the Cu(btmgp)I copper-complex to build a calibration relation with the corresponding grey-levels recorded by the camera. The colored signal comes from the consecutive reaction shown in Fig. 1, where the colorless initial Cu(I) complex is totally converted into the green Cu(II) complexes after few seconds. Note that between these initial and final states, one can observe the orange color from the Cu(III) complex. Unfortunately, the decay from the orange Cu(III) complex to the green Cu(II)-complexes is so fast at ambient temperature (the rate of decay is about 1.3 s^{-1} , Schurr et al., 2016) that this orange signal can only be captured in the vicinity and in the near-field wake of the bubble for a short period of time. The collection of raw images in Fig. 4 using the blue bandpass filter clearly shows this effect, as enabling to increase the contrast ratio and the signal-to-noise ratio (SNR) for the orange Cu(III) complex. In such conditions, it is impossible to get an exploitable signal from the grey-level values as the latter correspond to a mixture of orange Cu(III) and green Cu(II) complexes (see Fig. 5). Therefore, a calibration under the orange color signal is not possible.

However, given the kinetics of the reaction, after 2.5 s, it can be assumed that the integrity of the colored signal comes from the green Cu(II) complexes in the far-field wake of the bubble

(see Fig. 5b). For this reason, the calibration curve will consider the green signal of the Cu(II) complex, and thus the red band-pass filter will be used (instead of a blue one).

The experimental campaign has then been split into two parts; the first one, by using the blue filter to visualize and to make a *qualitative analysis* of the mass transfer in the near-field of the bubble; and the second one, by using the red filter to *quantify the gap-averaged oxygen mass transfer* in the far-field of the bubble.

This calibration procedure (namely the saturation of the cell in oxygen) is carried out at different mass concentrations of the initial Cu(I) complex, C_{Cu} , from 0 to $C_{Cu,max}$, to obtain the whole calibration curve, relating the equivalent oxygen concentration that is consumed by the reaction to a grey-level. As in Dietrich et al. (2013), one should use the term “equivalent” for the oxygen concentration as the latter is actually zero (consumed by the chemical reaction). $C_{Cu,max}$ is chosen to fit with the pure oxygen solubility in pure acetonitrile, $C_{O_2}^*$, equal to $259 \text{ mg} \cdot \text{L}^{-1}$. Considering the molar mass for the Cu(I) complex $M_{Cu} = 460.88 \text{ g mol}^{-1}$ and the molar mass for the oxygen $M_{O_2} = 32 \text{ g mol}^{-1}$, one can obtain $C_{Cu,max} = 7.37 \text{ g L}^{-1}$, knowing the stoichiometry of the reaction (see Fig. 1) by using the following relation:

$$C_{O_2} = \frac{1}{2} C_{Cu} \frac{M_{O_2}}{M_{Cu}}. \quad (4)$$

To account for each calibration point, Fig. 6 shows explicitly the change of the saturated grey-level signal in the region-of-interest window as a function of the initial concentration of Cu(I) complex;

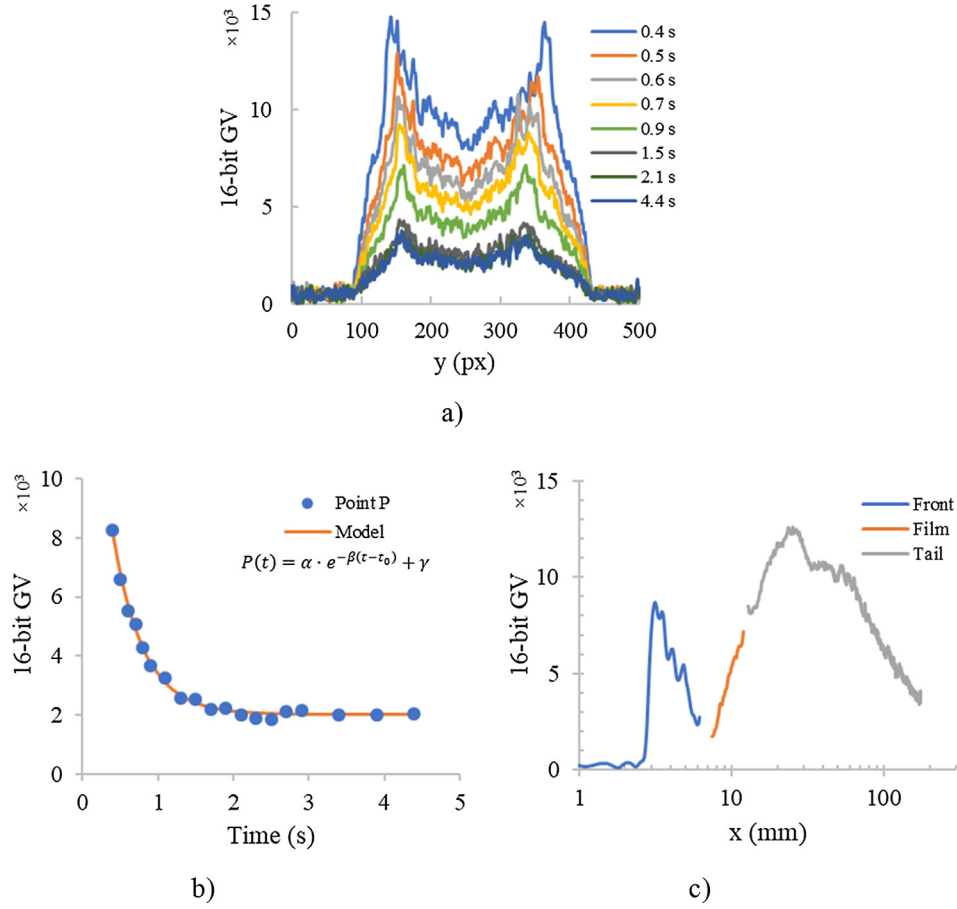


Fig. 5. Profiles extracted from Fig. 4d (a) Temporal evolution of a transversal grey-level profile along line A across the far-field wake. (b) Temporal evolution of grey-level value behind the bubble at the intersection of lines A and B (Point "P"). The initial time t_0 is associated to the bubble centroid passage, and the parameter β to the exponential decay rate. (c) Instantaneous grey-level profile along line B (including bubble passage).

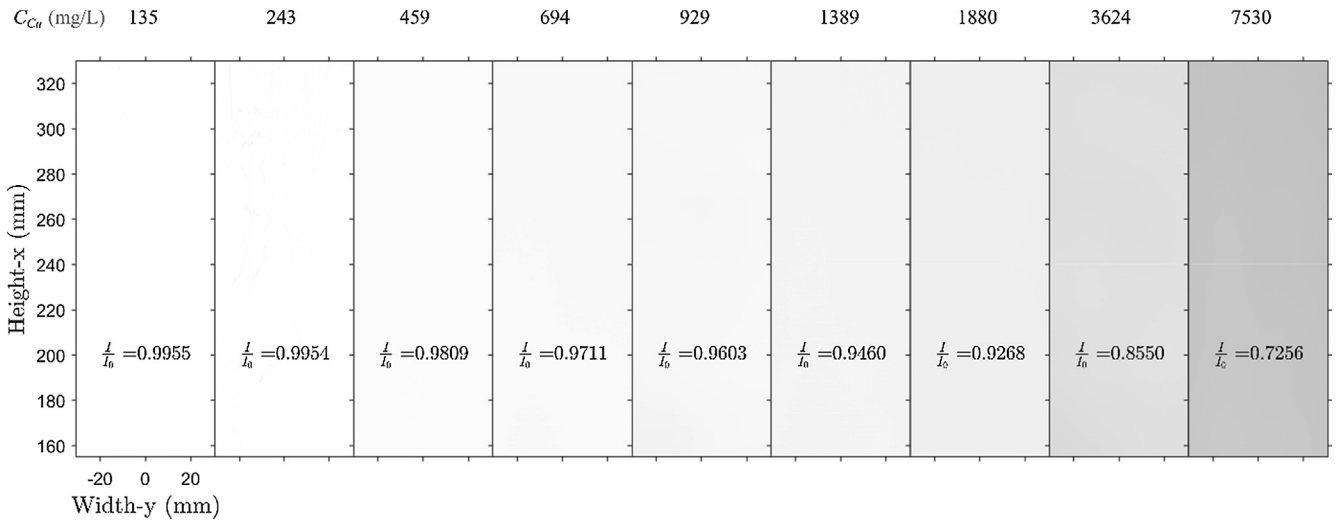


Fig. 6. Variation of the observed grey-level signal in the visualization window of the thin-gap cell as a function of the molar concentrations of the Cu(btmgp)I copper-complex.

for each case (i.e. on each image), the window-averaged transmittance $T = I/I_0$ is reported, where I is the 16-bit pixel-by-pixel intensity and I_0 the intensity of the background previously acquired. One can observe that the transmittance logically decreases with increasing initial concentration of Cu(I) complex.

The effective normalized absorption signal A is extracted at each concentration point, according to:

$$A = \frac{I_0 - I}{I_0} \quad (5)$$

where I_{00} is a normalisation parameter equal to the maximum 16-bit pixel intensity ($I_{00} = 2^{16} - 1$). This arbitrary choice is motivated to account for the dynamic range of the images; it acts only as a scale parameter. This signal A is then associated to the equivalent C_{O_2} , which is calculated from the initial concentration of Cu(I) complex C_{Cu} by using Eq. (4). The resulting calibration relation is shown in Fig. 7, where all the experimental points obtained from the averaged ROI windows in Fig. 6 are plotted against the equivalent oxygen concentration C_{O_2} . The calibration curve deduced from the fitting within these points follows an exponential law (as classically observed to describe light attenuation in an absorbing medium):

$$C_{O_2} = 707.826 \cdot (e^{1.708A} - 1). \quad (6)$$

This calibration method allows to convert a grey-level signal (A) into an equivalent gap-averaged oxygen concentration C_{O_2} , in the same way as applied in the original work by Dietrich et al. (2013) for the resazurin-based reactive solution. Nevertheless, it should be kept in mind that in the present case, the calibration is only valid in regions of the cell where all orange Cu(III) complex has been converted (i.e. where the consecutive reaction is complete). As previously presented, this is the case only in the far-field wake of the bubbles. No calibration can be here carried out for the instantaneous near-field around the bubbles shown in Fig. 4, contrary to the resazurin case studied by Dietrich et al. (2013). In addition, as the measured grey-level signals are located in the linear part of the calibration, it is possible to use it even with an inhomogeneous distribution of chemical species across the gap, and thus to convert a mean value of A into a gap-averaged equivalent oxygen concentration.

The available data are then concentrated in the far-field wake. Using the red band-pass filter, a significant increase in the contrast ratio and SNR can be obtained for the green Cu(II)-complex signal. Although no explicit calculation was provided, one observes that for all the studied cases (i.e. the bubble sizes), when using this red filter, the signal was always present even for the smallest bubbles, which was not the case with the blue filter. To ensure that there is no orange Cu(III) complex left, the images are acquired after 4 s from when the bubble reaches the ROI top boundary (see Fig. 5); then, the resulting signal is an average over 1 s (100 frames) when the liquid is totally at rest. This time averaging enables to reduce the random noise level of the imaging system, and is representative of constant instantaneous distribution because all motions have been killed by shear stress at the walls.

Fig. 8 thus shows the fixed signature of the mass transfer in the wake of a bubble rising from left-to-right. As mentioned before, the GV is here related to the Cu(II) species, which signal is increased by the use of the red filter (when compared to the cases without filter and with the previous blue filter), and averaged over 1 s, enhancing the quality for image post-processing.

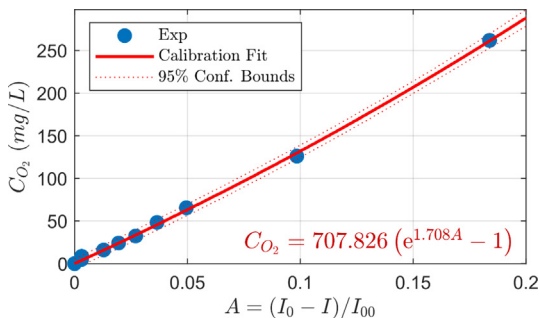


Fig. 7. Calibration fit of the observed grey-level signal to the equivalent gap-averaged oxygen concentration ($R^2 = 0.999$).

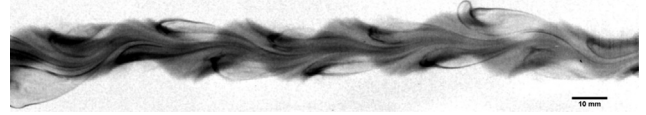


Fig. 8. Example of the enhanced grey-level signal from the green Cu(II) complexes after 4 s under a red band-pass filter. The result is a time-averaged value over $\Delta t = 1$ s. The bubble rises from left to right.

Finally, the effective absorption signal A is extracted from Fig. 8; then, applying the calibration relationship (from Eq. (5)), the equivalent oxygen concentration field in the far-field wake of the bubble, which is gap-averaged and time-averaged, can be deduced.

All the experiments to investigate mass transfer are performed with an initial concentration of Cu(I) complex equal to 7.53 g L^{-1} , which is close to $C_{Cu,max}$ corresponding equivalent oxygen solubility in pure acetonitrile using Eq. (4).

4. Results and discussion

4.1. Bubble dynamics

As reported in Table 1, the bubbles generated have diameters ranging from 3 mm to 20 mm. They are thus larger than the gap-width, $h/d < 1$, meaning that the bubbles are flattened in between the walls and adopt in-plane motions while rising with a velocity V_b . In the investigated conditions, the Archimedes number, Ar , and the Bond number, Bo , defined by Eq. (7), range from 860 to 18,800, and, from 1.8 to 108, respectively.

$$Ar = \frac{\rho_L \sqrt{g} d d}{\mu_L} \quad \text{and} \quad Bo = \frac{\rho_L g d^2}{\sigma} \quad (7)$$

Ar being always high and Bo moderate when varying the bubble diameter, contrasted regimes of oscillatory motions are observed, as in Filella et al. (2015) and in Roig et al. (2012). This is illustrated on the images gathered in Fig. 4 (see also videos on supporting information), where the transport of oxygen is an indirect measurement of the fluctuating nature of the velocity induced in the fluid around the bubble and in particular in its wake. For the smallest bubble, the path is unsteady and oxygen is collected by the released vortices, then, when the diameter increases, shape oscillations superpose to path ones and modulate the unsteady wake that may eventually re-stabilize for the largest bubbles. A strong destabilization of the preceding transverse vortices leading to the halo in front of the bubble is also observed for the larger bubble in Fig. 4. It is not clear if this happens only due to the high Reynolds number associated to this bubble or if it could be coupled with shape oscillations.

The variation of the bubble Reynolds number Re , as a function of the Archimedes number Ar , and the variation of the bubble aspect ratio, χ , as a function of the Weber number We , are reported in Fig. 9a and b respectively. The latter dimensionless numbers are defined as:

$$Re = \frac{\rho_L V_b d}{\mu_L} \quad \text{and} \quad We = \frac{\rho_L V_b^2 d}{\sigma} \quad (8)$$

Fig. 9: (a) Variation of the bubble Reynolds number Re as a function of the Archimedes number Ar . (b) Variation of the aspect ratio χ as a function of the Weber number We . The values of Filella et al. (2015) obtained in water with a gap of 3 mm are reported as well as the ones of Roudet et al. (2017) also obtained in water but with a gap of 1 mm.

In both figures, the dynamics of the bubble are compared to the ones reported by Roudet et al. (2017) and Filella et al. (2015) obtained in water with different gaps. A good agreement is

Table 1

Experimental results obtained, characterizing the bubble dynamics and the mass transfer.

Bubble #	$V_b(\text{m.s}^{-1})$	$(d)(\text{m})$	$(S_f) \times 10^6 (\text{m}^2)$	$(S_p) \times 10^6 (\text{m}^2)$	$\langle \phi \rangle (\text{mg.s}^{-1})$	$\langle \phi \rangle (\text{mg.m}^{-2}.\text{s}^{-1})$	$\chi(-)$	$Pe(\times 10^{-5})$	$Sh(-)$
1	0.157	0.0083	107.7	29.1	0.0112	81.9	2.92	1.42	284.8
2	0.124	0.0041	26.0	11.9	0.0030	77.3	1.64	0.55	132.0
3	0.190	0.0175	482.3	64.3	0.0778	142.2	2.98	3.61	1045.6
4	0.124	0.0040	25.1	11.7	0.0032	87.1	1.63	0.54	146.0
5	0.168	0.0132	274.4	49.3	0.0506	156.4	3.20	2.41	867.5
6	0.131	0.0045	32.0	13.4	0.0048	105.0	1.70	0.64	198.9
7	0.194	0.0201	634.0	75.3	0.0980	137.9	3.10	4.24	1162.5
8	0.107	0.0026	10.4	7.2	0.0005	29.3	1.27	0.30	31.6
9	0.153	0.0072	80.4	24.3	0.0141	134.5	2.71	1.19	403.8
10	0.158	0.0096	144.5	34.5	0.0236	131.3	2.76	1.65	528.5
11	0.154	0.0068	73.1	22.7	0.0123	127.4	2.56	1.14	364.8
12	0.172	0.0137	294.9	50.5	0.0522	150.9	3.05	2.56	867.5
13	0.180	0.0154	374.2	56.9	0.0629	145.7	2.98	3.02	943.7
14	0.118	0.0038	22.3	10.9	0.0032	95.3	1.53	0.48	150.7

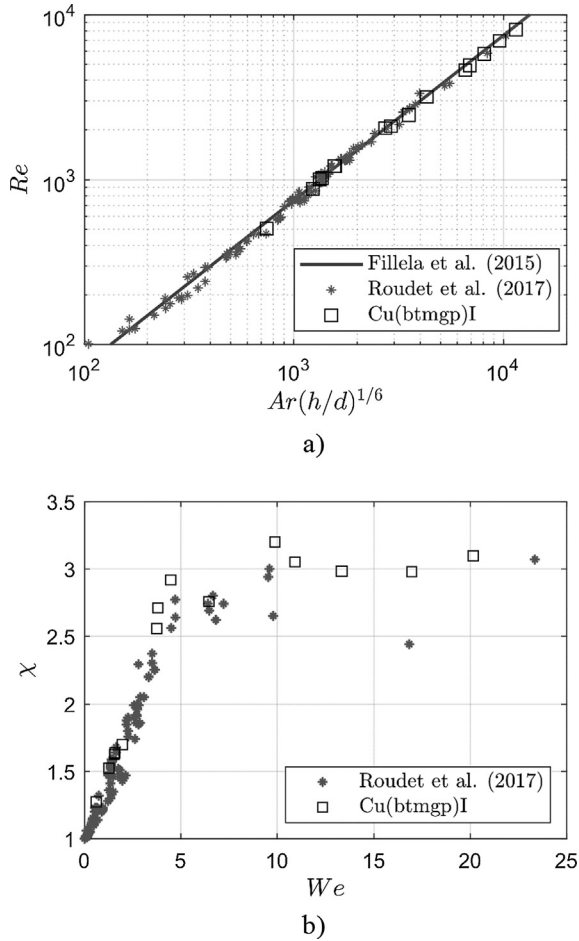


Fig. 9. (a) Variation of the bubble Reynolds number Re as a function of the Archimedes number Ar . (b) Variation of the aspect ratio χ as a function of the Weber number We . The values of Fillella et al. (2015) obtained in water with a gap of 3 mm are reported as well as the ones of Roudet et al. (2017) also obtained in water but with a gap of 1 mm.

observed with the scaling law proposed by these authors for Re (Eq. (9)), proving similar inertial regime in both studies:

$$Re = 0.75 \left(\frac{h}{d} \right)^{1/6} Ar \quad (9)$$

This relation connects the velocity of the bubble to its diameter and to the gap thickness. It indicates that there is no drag forces exerted by the liquid films (Roig et al., 2012) and that a slip condition probably exists at the clean bubble interfaces. It is

interesting to notice that the smaller dimensions, H and W , of the present cell as compared to that used by Roig et al. (2012) do not change the mean velocity of the bubble.

The aspect ratio χ reported on Fig. 9b is an important parameter that may be useful for general scaling of mass transfer. For a given diameter, bubbles were observed as more flattened in acetonitrile than in water due to the strong difference of surface tension between these two liquid phases ($\frac{\sigma_{cu}}{\sigma_w} = 0.78$). In the present study, the aspect ratio ranges between 1.2 and 3.2 (see Table 1 and Fig. 9b), and varies with the Weber number similarly for water and copper complex solution at moderate Weber number. However, asymptotic higher maximum values of the deformation are obtained in the present case at large Weber numbers. Acetonitrile having a lower surface tension, strong shape oscillations may also be observed for the largest bubbles for which we could not observe hemi-cylindrical stationary shapes as in water (see supporting information for Fig. 4e). The decreased viscosity of acetonitrile, as compared to water, also explains the appearance of original strongly destabilized and multi-scale vorticity revealed by the oxygen concentration fields for similar Archimedes numbers (Fig. 4e).

4.2. Concentration fields

Fig. 10 presents three examples of equivalent oxygen concentration fields in the far-field wake of oxygen bubbles. It is recalled that these concentrations are gap-averaged and time-averaged in a temporal sequence where no motion subsists (Section 3.2). As expected,

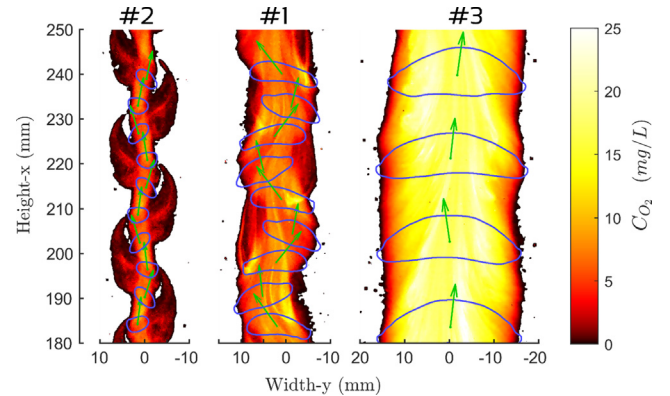


Fig. 10. Equivalent gap-averaged and time-averaged oxygen concentration in the wake of several oxygen bubbles (numbers # from Table 1). Bubble's ghosts are shown in blue contours and velocity vector in green arrows. For bubbles #1 and #2 $\Delta t = 0.05$ s and for bubble #3 $\Delta t = 0.1$ s. From left to right, the Archimedes number Ar is equal to 1711 (bubble #2, $d = 4.1$ mm), 4971 (bubble #1, $d = 8.3$ mm) and 15,300 (bubble #3, $d = 17.5$ mm). (For interpretation of the references to color in this figure legend, the reader is referred to the web version of this article.)

the contrasted bubble diameters previously described have a strong impact on the oxygen deposit, both in amount and in topology. These measured concentration fields result from the interfacial mass transfer taking place in two regions of contrasted flow dynamics: in the thin liquid films and in the high-Reynolds number in-plane flow in the vicinity of the bubble (Roudet et al., 2017). From Fig. 5c, it can be observed that a layer of high grey-level values (almost 3 mm in thickness in this case) exists in front of the bubbles, which grows with the characteristic bubble diameter (as mentioned, this signal cannot be quantitatively correlated to equivalent oxygen concentration, due to the fast decay of the orange Cu(III) complex, see Section 3.2). According to Roudet et al. (2017) who also visualized such layer by PLIF-I investigations, these halos at the front might be related to vortices produced by the confinement of the bubble. Although the exact origin of this phenomenon is not completely understood yet, the time-series of Fig. 4 (see videos on supporting information) show that the oxygen transferred at this peripheral interfacial region is transported by the flow all around the bubble, to be then recombined by layers with the amount transferred at the liquid films inside the 1 mm gap, leading to the complex deposit in the wake shown in Fig. 10. To identify the contribution of each mechanism, information about the dynamics of the films and the flow around and past the bubble is required.

It is interesting to note that, for the smaller bubble (#2 in Fig. 10), the equivalent oxygen field presents a complex periodic pattern combined with a nearly straight stripe, the amount of oxygen being smaller inside the periodic structures than in the bulk of the stripe. However, for larger bubbles (bubbles #1 and #3 in Fig. 10), only a slightly oscillating stripe is observed relative to the bubble size, characterized by high values of oxygen concentration (up to 20 mg L^{-1}). This diversity of features is consistent with what is known concerning the bubble dynamics, and in particular with the evolution of its wake, which is steady for $Ar < 100$, unsteady and periodic for Archimedes numbers in the range $100 - 10,000$, and steady again and for $Ar > 10,000$ (Roig et al., 2012). The present results are also in agreement with the averaged PLIF images of Roudet et al. (2017) where there was no chemical reaction. This means that despite the presence of a chemical reaction, once the oxygen is transferred at the interface, its transport in the velocity perturbation generated by the bubble is similar to the case without reaction. The presence of the chemical reaction can nevertheless change the amount of oxygen transferred at the interface. One should notice, in particular from Fig. 10 that provides planar distributions of concentration, that when the bubble diameter increases, higher concentration values are more and more present. This indicates that the mass transfer rate increases not only due to a larger area of the interface but also due to an intensification of the mass flux.

4.3. Mass flux and Sherwood number

From these concentration fields, the equivalent oxygen mass flux can be determined using a similar procedure as in Roudet et al. (2017). The total mass transfer rate $\langle \phi \rangle$ from the bubble is the mass of oxygen $m(t)$ deposited in a window of observation at a given time t , divided by the time spent by the bubble to cross this window. To achieve this, the equivalent gap- and time-averaged concentration \bar{C}_{O_2} , from Fig. 10 is combined with the bubble position and velocity to reconstruct a $m(t)$ time-series. At a given time, the measured total oxygen mass in any frame (like in Fig. 10) is the volume integral over the concentration field C_{O_2} . However, because these fields are fixed in time, an artificial time signal is used by integrating only up from the previous position of the bubble. Then, a variable integration window of constant horizontal extension defined for the whole ROI and of variable vertical extension $L(t)$ is defined from the origin up to the centroid x -position; therefore,

$L(t)$ grows as $V_b(t)$ and the integration is made over the resulting image as follows:

$$m(t) = h \iint_0^{L(t)} \bar{C}_{O_2}(x, y) dx dy, \quad (10)$$

resulting in $m(t)$ calculated with a temporal resolution equal to image frame-rate of 0.01 s. Compared to the extreme case of Roudet et al. (2017), this method is purely a refinement because of the temporal resolution, as it allows to capture some of the fluctuating part of the mass transfer. Then, the total average mass flux $\langle \phi \rangle$ is obtained from the numerical time-derivative of these ever growing $m(t)$, averaged over the time period signal:

$$\langle \phi \rangle = \left\langle \frac{d}{dt} m(t) \right\rangle. \quad (11)$$

Although the fluctuating part is partially captured, this information is killed by the time-average afterwards (i.e. when $\langle \phi \rangle$ is calculated). Nevertheless, this fluctuation is kept to represent an error bar around the mean values. Using this, the mass flux density $\langle \phi \rangle$ is obtained from simply dividing $\langle \phi \rangle$ by the estimated total gas-liquid interface S_T :

$$\langle \phi \rangle = \frac{\langle \phi \rangle}{S_T}. \quad (12)$$

where S_T is the total area of the bubble gas-liquid interface defined as $S_T = S_p + S_f$, with S_p and S_f the areas of the peripheral interface in contact with the in-plane flow and on the liquid films respectively (see Eq. (3) and Table 1). This definition of $\langle \phi \rangle$ represents the global mass flux density, resulting from the oxygen transferred from the thin liquid films and in the external region around the bubble.

To normalize this mass flux density, a Sherwood number, Sh , can be introduced, its definition being based on the diameter of the bubble d :

$$Sh = \frac{\langle \phi \rangle d}{\mathfrak{D}_{O_2} C_{O_2}^*}. \quad (13)$$

Fig. 11 reports the variation of the Sherwood number Sh as a function of the Peclet number Pe , as defined as:

$$Pe = \frac{V_b d}{\mathfrak{D}_{O_2}}. \quad (14)$$

Mass flux, velocity and bubble sizes variations are gathered to represent the error bars in Fig. 11, where the error is taken as the root-mean-squared value around the respective Sh and Pe calculated numbers. In Table 1 are reported, for each bubble, the mass flux $\langle \phi \rangle$, the areas of the peripheral interface in contact with the in-plane flow and on the liquid films, S_p and S_f , the mass flux density $\langle \phi \rangle$, the Sherwood and Peclet numbers, Sh and Pe .

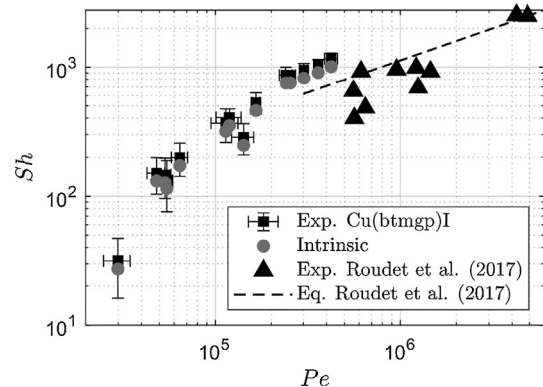


Fig. 11. Estimated Sherwood number (Sh) as a function of the Peclet number (Pe). The experimental data found by Roudet et al. (2017) obtained in water with a gap of 1 mm are reported as a reference.

Fig. 11 shows how strong mass transfer is favored by increasing Peclet number. As a reference, the experimental data determined by Roudet et al. (2017) in water are reported, which followed the relation $Sh = 1.126 \cdot Pe^{0.5}$. This scaling law does not fully describe the present experimental results obtained in an organic liquid phase (copper complexes dissolved in acetonitrile). At large Peclet numbers (greater than $2 \cdot 10^5$), the slope is similar but the Sherwood numbers are greater. Then, when Pe decreases, a sharper decrease of Sh is observed. Several reasons may be raised to explain the difference observed between the present results and those reported for experiments performed in water (Roudet et al., 2017). First, the physico-chemical properties of water are not similar to those of copper-complex acetonitrile solutions, as reported below:

$$\frac{v_{Cu}}{v_w} = 0.43; \quad \frac{\rho_{Cu}}{\rho_w} = 0.78; \quad \frac{\sigma_{Cu}}{\sigma_w} = 0.78 \quad (15)$$

This leads to a change in the Schmidt number $Sc = \nu/D$ from = 52 in the present case to 348 in water, which could significantly impact the mass transfer.

In addition, as the kinetic rate of the formation of the Cu(III) complex from the Cu(I) complex is fast, one should not exclude a possible enhancement of the mass transfer by the reaction. If it occurs, the measured Sherwood numbers would correspond to *enhanced* Sherwood numbers, and not *intrinsic* Sherwood number (namely corresponding to pure absorption). To quantify this, the enhancement factor E needs to be evaluated.

4.4. Enhancement factor

To estimate the enhancement factor E , the Hatta number Ha has to be first calculated as its value points out the reactional regime in which the experiments take place. Each regime is characterized by specific properties, indicating where the reaction occurs (in the liquid film, in the liquid bulk or in both regions) and if the mass transfer flux is enhanced by the reaction (Roizard et al., 1997; Levenspiel, 1999). In that objective, the kinetic law of the reaction between Cu(I) and Cu(III) complexes has to be known as well as the diffusion coefficient of the copper complex in acetonitrile.

4.4.1. Kinetics for the Cu(III) complex formation

According to Strassl (2019), the kinetics of the formation of the Cu(III) complex is of second order, and can be expressed as:

$$r = k \cdot C_{Cu} \cdot C_{O_2}. \quad (16)$$

where k is the second-order kinetic constant ($L \cdot mol^{-1} \cdot s^{-1}$), C_{Cu} is the concentration of the Cu(I) complex and C_{O_2} the oxygen concentration.

Strassl (2019) determined the constant kinetic using a stopped-flow set-up at ambient temperature (as in Schurr et al., 2016), and under excess of oxygen. Under such conditions, he obtained an apparent kinetics constant, k_{app} , equal to $30 \pm 4 \text{ s}^{-1}$, this constant corresponding to

$$k_{app} = k \cdot C_{O_2}^*. \quad (17)$$

Knowing that the solubility of oxygen in acetonitrile is $C_{O_2}^* = 8.09 \times 10^{-3} \text{ mol} \cdot L^{-1}$, it becomes:

$$k = 3707 \pm 500 \text{ L} \cdot \text{mol}^{-1} \cdot \text{s}^{-1}. \quad (18)$$

4.4.2. Diffusion coefficient of Cu(I) complex

The diffusion coefficient of the Cu(I) complex is determined by the 2D-NMR technique diffusion ordered spectroscopy (DOSY). A DOSY measurement uses pulsed-field-gradient NMR to apply a varying magnetic field. Then, the movement of molecules in

relation to the locally varying magnetic field is followed by a spin-echo experiment. The varying magnetic field leads to different intensities of the examined molecules. NMR intensities originating from moving molecules, in relation to the local magnetic fields are obtained which then provide information about the diffusion.

A solution of the Cu(I) complex in dried and deuterated acetonitrile under inert gas is prepared in a gas-tight Young NMR tube. The NMR spectroscopy is performed at a temperature of $24 \text{ }^\circ\text{C}$ (297 K). The diffusion coefficient of the copper complex is determined, by the Bruker program Dynamics Center (Bruker Biospin, Dynamics Center 2.4.8, Billerica, Massachusetts, USA, 2016), as:

$$\mathfrak{D}_{Cu} = (1.40 \pm 0.05) \times 10^{-9} \text{ m}^2 \cdot \text{s}^{-1}. \quad (19)$$

In the same measurement, the diffusion coefficient of acetonitrile was determined by the residual solvent signal as $(4.2 \pm 0.3) \times 10^{-9} \text{ m}^2 \cdot \text{s}^{-1}$. A diffusion coefficient for acetonitrile of $(4.34 \pm 0.3) \times 10^{-9} \text{ m}^2 \cdot \text{s}^{-1}$ at a temperature of 298 K has been determined by a diaphragm earlier (Easteal and Woolf, 1984). The exactly matching diffusion coefficients of acetonitrile indicate an accurate determination of the diffusion coefficient of the Cu(I) complex.

4.4.3. Estimation of the Hatta number and enhancement factor

As already explained, the reaction system involves two consecutive reactions: in the first reaction, the Cu(I) complex oxidizes into Cu(III) complex, and in the second reaction, the Cu(III) complex decays into Cu(II) complexes. Nevertheless, the competition between mass transfer and reaction exists only for the first reaction, the oxygen being not involved in the second reaction. Therefore, one should consider calculating the Hatta number only for the first reaction which is of second order. In this case, the Hatta number can be expressed as (Roizard et al., 1997; Levenspiel, 1999):

$$Ha = \frac{\sqrt{k \cdot C_{Cu,0} \cdot \mathfrak{D}_{O_2}}}{k_L}; \quad (20)$$

where \mathfrak{D}_{O_2} is the diffusion coefficient of oxygen, $C_{Cu,0}$ is the initial molar concentration of the Cu(I) complex used in the experiments (namely $7.530 \text{ g} \cdot L^{-1} \equiv 0.0163 \text{ mol} \cdot L^{-1}$) and k_L is the liquid-side mass transfer coefficient.

Then, the approximate solution (implicit form) proposed by Van Krevelen and Hoftijzer (1948) is used to estimate the enhancement factor:

$$E = \frac{Ha \sqrt{\frac{E_i - E}{E_i - 1}}}{\tanh\left(Ha \sqrt{\frac{E_i - E}{E_i - 1}}\right)}; \quad (21)$$

where E_i is the limit enhancement factor defined by

$$E_i = 1 + \frac{\mathfrak{D}_{Cu} C_{Cu,0}}{2 \mathfrak{D}_{O_2} C_{O_2}^*}. \quad (22)$$

It comes $E_i = 1.15$.

The liquid-side mass transfer coefficient can be evaluated from the following equation:

$$k_L = \frac{Sh \cdot d}{E \cdot \mathfrak{D}_{O_2}} = \frac{\langle \varphi \rangle}{E \cdot C_{O_2}^*}; \quad (23)$$

where Sh is the measured Sherwood number. As the latter can be possibly enhanced by the reaction, the mass flux should be divided by the enhancement factor in Eq. (23). As a consequence, an iterative procedure is implemented to calculate the Hatta number and the enhancement factor.

The Hatta number is found to be of the order of 7.6 for the smallest bubble ($d = 2.6 \text{ mm}$), implying that the reaction occurs entirely in the film. For the other bubbles, the Hatta number is

ranged between 1.4 ($d \sim 13$ mm) and 2.9 ($d \sim 4$ mm): in these cases, one part of the reaction occurs in the film and the other part in the liquid bulk. Whatever the bubble diameters, the enhancement factor remains ranged between 1.12 and 1.15.

Knowing E , the enhanced Sherwood numbers (namely the ones measured using the copper complex colorimetric method) can be converted into *intrinsic* Sherwood numbers (associated to diffusive mass transfer), such as:

$$Sh_{\text{intrinsic}} = \frac{Sh_{\text{enhanced}}}{E}. \quad (24)$$

They are also plotted in Fig. 11. From this, it can be deduced that the reaction induces an over-estimation of about 12–15% of the measured Sherwood numbers. The physical variation ranges of the Sherwood and Peclet numbers are also reported in Fig. 11 for each point: they are related to the unsteady properties of the phenomena, and in particular to the oscillations of the bubble path. It can be observed that they are of the same order of magnitude than the decrease due to the reaction (12–15%). This would suggest that the enhancement of the mass transfer by the reaction has not a major effect and is not the main mechanism responsible for the difference with the scaling law proposed by Roudet et al. (2017). As mentioned, changes in Schmidt numbers and bubbles shape may explain a part of the difference. However, this conclusion should be taken with care. Indeed, the Hatta number and the enhancement factor, previously determined, are averaged (global) values as calculated from gap-averaged and time-averaged concentration fields measured in the far-field wake of the bubbles, and thus from averaged (global) Sherwood number. In fact, a spatio-temporal distribution of the Hatta number and of the enhancement factors exists because the mass transfer mechanism, and the transferred oxygen fluxes, are not the same in the liquid film close to the bubble or in the near-wake or far-wake of the bubble. Unfortunately, such information (i.e. the time-resolved oxygen concentration field) is not experimentally accessible so far.

5. Conclusion

In this experimental study, the oxygen mass transfer around a single bubble rising at large Reynolds number in a thin-gap cell was investigated in the presence of consecutive chemical reactions. A colorimetric method was used to track the products of the reactions and thus to obtain, from stoichiometry arguments, the mass of oxygen that was transferred at the gas-liquid interface. The chemical system consisted in a bio-inspired copper complex, Cu (btm₂gp)I, specially tailored, which, dissolved in acetonitrile, oxidized into an orange copper-complex $[Cu_2O_2(btm_2gp)_2]I_2$, the latter complex decaying quite fast into two Cu(II) complexes (pale-green colour). An image acquisition system (based on the use of specific optical filters) was used, combined with an ad hoc calibration protocol, to correlate the grey-levels from the coloured signal to the equivalent oxygen concentrations, while tracking the bubble motion and properties. At last, it was possible to measure the equivalent gap-averaged and time-averaged oxygen concentration fields in the far-field at rest in the wake of the bubble.

The contrasted hydrodynamic regimes observed had a strong impact on the oxygen deposit, both in amount and in topology. The bubbles motion is found to follow a specific scaling law of the terminal velocity as a function of the characteristic size and gap thickness (represented as $Re = \mathcal{F}(Ar)$), in the same way like in other studies using water with different geometries of the confining cell, evincing the inertial regime and that no drag forces are exerted by the liquid films. Combining the observed bubble dynamics with the calculated mass transfer, the obtained Sherwood number varied with the Peclet number with a scaling law

that recovered the one reported by Roudet et al. (2017), $Sh \sim Pe^{0.5}$, (obtained by PLIFI investigations in water and without chemical reaction) at least at large Peclet numbers. Measurements were also obtained at smaller Peclet numbers and revealed that the scaling law changes for such values. However, the Sherwood numbers were here slightly over-estimated due the occurrence of an enhancement of the mass transfer by the reaction (the enhancement factor E was estimated to 1.12–1.15). Even with this correction, the Sherwood numbers associated to purely physical absorption do not perfectly collapse at high Peclet numbers. The origin of the difference between both studies could come from sensitivity of the problem to Schmidt numbers that were different. Indeed, the relation $Sh = \mathcal{F}(Pe)$ does not include the variation of the surface tension, which is found to shift the regime of the average aspect ratio as a function of the Weber number, an effect that might add another dimension to this type of analysis.

In future work, new experiments must be carried out, in particular with other solvents, so as to enlarge the range of considered Peclet numbers and also to reach different values of the Schmidt number. In order to have a better description of the reactive mass transfer, it will be important to follow the temporal evolution of Cu(III) and Cu (II) complexes simultaneously. While one can think about measuring both concentrations using two cameras with different filters, the key hard challenge will remain the calibration relation between the grey level associated to the Cu(III) complex concentration as this product decays quite quickly. Using other bio-inspired copper complexes, offering different reaction schemes and kinetics, will be a promising solution to deeply investigate the competition between interfacial mass transfer and reaction selectivity.

Declaration of Competing Interest

Author declares that there is no conflict of interest.

Acknowledgements

The authors gratefully acknowledge the financial support provided by the CNRS Research Federation FERMaT (FR 3089) in Toulouse and by the German Research Foundation within the Priority Program « Reactive Bubbly flows » SPP 1740. Sonja Herres-Pawlis thanks the Deutsche Forschungsgemeinschaft for generous support (SPP1740, HE5480/10-2).

The authors thank the laboratory LCC (CNRS UPR 8241), and especially Dr. Rosa Axet, for allowing the use of their glovebox.

The authors acknowledge Alain Pontier, Grégory Ehes and Jack Compain for their technical support, and Emmanuel Cid and Claude Lemen for their help concerning the image acquisition system.

This paper is dedicated to the memory of Dr. Matthieu Roudet, who was a pioneering young collaborator in the investigation of bubbly flows in thin-gap cell, and who tragically disappeared. He will remain in the minds of the authors.

Appendix A. Supplementary material

Supplementary data to this article can be found online at <https://doi.org/10.1016/j.ces.2019.07.045>.

References

- Achord, J.M., Hussey, C.L., 1980. Determination of dissolved oxygen in nonaqueous electrochemical solvents. *Anal. Chem.* 52 (3), 601–602.
- Almeras, E., Cazin, S., Risso, F., Roig, V., Augier, F., Plais, C., 2016. Time-resolved measurement of concentration fluctuations in a confined bubbly flow by LIF. *Int. J. Multiph. Flow* 83, 153–161. <https://doi.org/10.1016/j.ijmultiphaseflow.2016.03.011>.

- Almeras, E., Risso, F., Roig, V., Plais, C., Augier, F., 2018. Mixing mechanism in a two-dimensional bubble column. *Phys. Rev. Fluids*, 3, 074307. <https://doi.org/10.1103/PhysRevFluids.3.074307>.
- Anxionnaz, Z., Cabassud, M., Gourdon, C., Tochon, R., 2008. Heat exchanger/reactors (HEX reactors): concepts, technologies: state-of-the-art. *Chem. Eng. Process. Process Intensif.* 47 (12), 2029–2205. <https://doi.org/10.1016/j.cep.2008.06.012>.
- Aussillous, P., Quéré, D., 2000. Quick deposition of a fluid on the wall of a tube. *Phys. Fluid.* 12 (10), 2367–2371. <https://doi.org/10.1063/1.1289396>.
- Bouche, E., Roig, V., Risso, F., Billet, A.M., 2012. Homogeneous swarm of high-Reynolds-number bubbles rising within a thin gap. Part 1. Bubble dynamics. *J. Fluid Mech.* 704, 211–231. <https://doi.org/10.1017/jfm.2012.233>.
- Bouche, E., Roig, V., Risso, F., Billet, A.M., 2014. Homogeneous swarm of high-Reynolds-number bubbles rising within a thin gap. Part 2. Liquid dynamics. *J. Fluid Mech.* 758, 508–521. <https://doi.org/10.1017/jfm.2014.544>.
- Butler, C., Cid, E., Billet, A.-M., 2016. Modelling of mass transfer in Taylor flow: investigation with the PLIF-technique. *Chem. Eng. Res. Des.* 115, 292–302. <https://doi.org/10.1016/j.cherd.2016.09.001>.
- Butler, C., Lalanne, B., Sandmann, K., Cid, E., Billet, A.-M., 2018. Mass transfer in Taylor flow: transfer rate modelling from measurements at the slug and film scale. *Int. J. Multiph. Flow* 105, 185–201. <https://doi.org/10.1016/j.ijmultiphaseflow.2018.04.005>.
- Citek, C., Herres-Pawlis, S., Stack, T.D.P., 2015. Low temperature syntheses and reactivity of Cu₂O₂ active-site models. *Acc. Chem. Res.* 48, 2424–2433. <https://doi.org/10.1021/acs.accounts.5b00220>.
- Dietrich, N., Loubière, K., Jimenez, M., Hébrard, G., Gourdon, C., 2013. A new direct technique for visualizing and measuring gas-liquid mass transfer around bubbles moving in a straight millimetric square channel. *Chem. Eng. Sci.* 100, 172–182. <https://doi.org/10.1016/j.ces.2013.03.041>.
- Eastale, A.J., Woolf, L.A., 1984. Solute-solvent interaction effects on tracer diffusion coefficients. *J. Chem. Soc., Faraday Trans. 1*, 80, 1287–1295. <https://doi.org/10.1039/F19848001287>.
- Falcone, M., Bothe, D., Marschall, H., 2018. 3D direct numerical simulations of reactive mass transfer from deformable single bubbles: an analysis of mass transfer coefficients and reaction selectivities. *Chem. Eng. Sci.* 177, 523–536. <https://doi.org/10.1016/j.ces.2017.11.024>.
- Filella, A., Ern, P., Roig, V., 2015. Oscillatory motion and wake of a bubble rising in a thin-gap cell. *J. Fluid Mech.* 778, 60–88. <https://doi.org/10.1017/jfm.2015.355>.
- Hamann, J.N., Herzigkeit, B., Jurgeleit, R., Tuzcek, F., 2017. Small-molecule models of tyrosinase: from ligand hydroxylation to catalytic monooxygenation of external substrates. *Coord. Chem. Rev.* 334, 54–66. <https://doi.org/10.1016/j.ccr.2016.07.009>.
- Herres-Pawlis, S., Heuwing, A.J., Flörke, U., Schneider, J., Henkel, G., 2005a. Hydroxylation of a methyl group: synthesis of [Cu₂(btmmO)₂]⁺ and of (Cu₂(btmmO)₂)²⁺ containing the novel ligand {bis(trimethylmethoxy)guanidine}propane (btmmO) by copper-assisted oxygen activation. *Inorg. Chim. Acta* 358, 1089–1095. <https://doi.org/10.1016/j.ica.2004.10.009>.
- Herres-Pawlis, S., Flörke, U., Henkel, G., 2005b. Tuning of copper(I)-dioxygen reactivity by bis(guanidine) ligands. *Eur. J. Inorg. Chem.* 19, 3815–3824. <https://doi.org/10.1002/ejic.200400822>.
- Hoffmann, A., Citek, C., Binder, S., Goos, A., Rübhausen, M., Troepner, O., Ivanović-Burmazović, I., Wasinger, E.C., Stack, T.D.P., Herres-Pawlis, S., 2013. Catalytic phenol hydroxylation with dioxygen: extension of the tyrosinase mechanism beyond the protein matrix. *Angew. Chem. Int. Ed. Engl.* 52, 5398–5401. <https://doi.org/10.1002/anie.201301249>.
- Jimenez, M., Dietrich, N., Hébrard, G., 2013. Mass transfer in the wake of non-spherical air bubbles quantified by quenching of fluorescence. *Chem. Eng. Sci.* 100, 160–171. <https://doi.org/10.1016/j.ces.2013.01.036>.
- Kastens, S., Timmermann, J., Tampmaier, R.F., Hoffmann, A., Herres-Pawlis, S., Schlüter, M., 2017. Test system for the investigation of reactive Taylor bubbles. *Chem. Eng. Technol.* 40 (8), 1–9. <https://doi.org/10.1002/ceat.201700047>.
- Kroneck, P. M. H., and Sosa Torres, M. E. (Eds), 2015. *Sustaining Life on Planet Earth: Metalloenzymes Mastering Dioxygen and Other Chewy Gases, Metals Ions in Life Sciences*. Volume 15, Springer International Publishing, Switzerland. ISBN 978-3-319-12415-5.
- Khinast, J.G., 2001. Impact of 2-D bubble dynamics on the selectivity of fast gas-liquid reactions. *AIChE J.* 47 (10), 2304–2319.
- Kováts, P., Pohl, D., Thévenin, D., Zähringer, K., 2018. Optical determination of oxygen mass transfer in a helically-coiled pipe compared to a straight horizontal tube. *Chem. Eng. Sci.* 190, 273–285. <https://doi.org/10.1016/j.ces.2018.06.029>.
- Levenspiel, O., 1999. *Chemical Reaction Engineering*. John Wiley & sons Inc.
- Li, Q., Batchelor-McAuley, C., Lawrence, N.S., Hartshorne, R.S., Compton, R.G., 2013. Anomalous solubility of oxygen in acetonitrile/water mixture containing tetra-n-butylammonium perchlorate supporting electrolyte. The solubility and diffusion coefficient in anhydrous acetonitrile and aqueous mixtures. *J. Electroanal. Chem.* 688, 328–335. <https://doi.org/10.1016/j.jelechem.2012.07.039>.
- Liebhäuser, P., Hoffmann, A., Herres-Pawlis, S., 2016. In Reference Module in chemistry, molecular sciences and engineering. *Synthesis, Spectroscopy, Theory and Catalysis, Tyrosinase Models*. 10.1016/B978-0-12-409547-2.11554-9. Doi:10.1002/chem.201785069.
- Liebhäuser, P., Keisers, K., Hoffmann, A., Schnappinger, T., Sommer, I., Thoma, A., Wilfer, C., Schoch, R., Stührenberg, K., Bauer, M., Dürr, M., Ivanović-Burmazović, I., Herres-Pawlis, S., 2017. Frontispiece: record broken: a copper peroxide complex with enhanced stability and faster hydroxylation catalysis. *Chem. Eur. J.* 23, 12171–12183.
- Martinez, F.L.D., Julcour, C., Billet, A.-M., Larachi, F., 2016. Modelling and simulations of a monolith reactor for three-phase hydrogenation reactions – rules and recommendations for mass transfer analysis. *Catal. Today* 273, 121–130. <https://doi.org/10.1016/j.cattod.2016.04.009>.
- Oelgemöller, M., 2016. Solar photochemical synthesis: from the beginnings of organic photochemistry to the solar manufacturing of commodity chemicals. *Chem. Rev.* 116 (17), 9664–9682. <https://doi.org/10.1021/acs.chemrev.5b00720>.
- Otsu, N., 1979. A threshold selection method from gray-level histograms. *IEEE Trans. Syst., Man, Cybern.* 9 (1), 6–66. 3 10.1109/TSMC.1979.4310076.
- Paul, M., Streissel, F., Hoffmann, M., Schlueter, M., Herres-Pawlis, S., 2018. Reaction systems for bubbly flows. *Europ. J. Inorgan. Chem.* 20–21, 2101–2124. <https://doi.org/10.1002/ejic.201800146>.
- Pruvost, J., Le Borgne, F., Artu, A., Legrand, J., 2017. Development of a thin-film solar photobioreactor with high biomass volumetric productivity (AlgoFilm©) based on process intensification principles. *Algal Res.* 21, 120–137. <https://doi.org/10.1016/j.algal.2016.10.012>.
- Radl, S., Koynov, A., Tryggvason, G., Khinast, J.G., 2008. DNS-based prediction of the selectivity of fast multiphase reactions: hydrogenation of nitroarenes. *Chem. Eng. Sci.* 63, 3279–3291. <https://doi.org/10.1016/j.ces.2008.03.025>.
- Rao, H., Schmidt, L.C., Bonin, J., Robert, M., 2017. Visible-light-driven methane formation from CO₂ with a molecular iron catalyst. *Nature* 548, 74–77. <https://doi.org/10.1038/nature23016>.
- Roig, V., Roudet, M., Risso, F., Billet, A.-M., 2012. Dynamics of a high Reynolds-number bubble rising within a thin gap. *J. Fluid Mech.* 707, 444–466. <https://doi.org/10.1017/jfm.2012.289>.
- Roizard, C., Wild, G., Charpentier, J.C., 1997. Absorption avec réaction chimique. *Tech. de l'Ingénieur. J 1 (079)*, 1–20.
- Roudet, M., Billet, A.-M., Cazin, S., Risso, F., Roig, V., 2017. Experimental investigation of interfacial mass transfer mechanisms for a confined high Reynolds-number bubble rising in a thin gap. *AIChE J.* 63 (6), 2394–2408. 13 10.1002/aic.15562.
- Rüttinger, S., Spille, C., Hoffmann, M., Schlüter, M., 2018. Laser-induced fluorescence in multiphase systems. *ChemBioEng Rev.* 5, 253–269. <https://doi.org/10.1002/cben.201800005>.
- Schurr, D., Strassl, F., Liebhäuser, P., Rinke, G., Dittmeyer, R., Herres-Pawlis, S., 2016. Decay kinetics of sensitive bioinorganic species in a SuperFocus mixer at ambient conditions. *React. Chem. Eng.* 1, 485–493. <https://doi.org/10.1039/c6re00119j>.
- Solomon, E.I., Heppner, D.E., Johnston, E.M., Ginsbach, J.W., Cirera, J., Qayyum, M., Kieber-Emmons, M.T., Kjaergaard, C.H., Hadt, R.G., Tian, L., 2014. Copper active sites in biology. *Chem. Rev.* 114, 3659–3853. <https://doi.org/10.1021/cr400327t>.
- Strassl, F. Copper, 2019. *Dioxygen Complexes for Multiphase Flows*. PhD thesis to be submitted. RWTH Aachen University.
- Thobie, C., Gadoin, E., Blel, W., Pruvost, J., Gentric, C., 2017. Global characterization of hydrodynamics and gas-liquid mass transfer in a thin-gap bubble column intended for microalgae cultivation. *Chem. Eng. Process.* 122, 76–89. <https://doi.org/10.1016/j.cep.2017.10.009>.
- Van Krevelen, D.W., Hoftijzer, P.J., 1948. Kinetics of gas-liquid reactions. *Recueils des Travaux Chimiques des Pays-Bas* 67, 563–586.
- Yang, L., Dietrich, N., Hébrard, G., Loubière, K., Gourdon, C., 2017. Optical methods to investigate the enhancement factor of an oxygen-sensitive colorimetric reaction using microreactors. *AIChE J.* 63, 2272–2284. <https://doi.org/10.1002/aic.15547>.
- Wilfer, C., Liebhäuser, P., Hoffmann, A., Erdmann, H., Grossmann, O., Runtsch, L., Pfaffenholz, E., Schepper, R., Dick, R., Bauer, M., Dürr, M., Ivanović-Burmazović, I., Herres-Pawlis, S., 2015. Efficient biomimetic hydroxylation catalysis with a bis(pyrazolyl)imidazolylmethane copper peroxide complex. *Chem. Eur. J.* 21, 17639–17649. <https://doi.org/10.1002/chem.201501685>.